A Spatial Near-Field Clutter Reduction Filter Preserving Tissue Speckle in Echocardiography

Marloes Sjoerdsma, *Member, IEEE*, Sjoerd Bouwmeester, Patrick Houthuizen, Frans N. van de Vosse, and Richard G. P. Lopata, *Senior Member, IEEE*

Abstract—Near-field (NF) clutter in echocardiography is depicted as a diffuse haze hindering the visualization of the myocardium and the blood-pool, thereby degrading its diagnostic value. Several clutter filters have been developed, which are limited in patients with contraction motion and rhythm anomalies, and in 3-D ultrasound (US). This study introduces a new NF clutter reduction method, which preserves US speckles required for strain imaging. The filter developed detects the NF clutter region in the spatial frequency domain. The filter employs an oriented, multiscale approach, and assumes the NF clutter to be predominantly present in the highest and lowest bandpass images. These bandpass images were filtered, whilst sparing features in the myocardium and NF clutter-free regions. The performance of the filter was assessed in a volunteer study, in ten 3-D apical and parasternal view acquisitions, and in a retrospective clinical study composed of 20 cardiac patients with different indications for echocardiography. The filter reduced NF clutter in all data sets, whilst preserving all or most of the myocardium. Additionally, it demonstrated a consistent enhancement of image quality, with an increase in contrast of 4.3 dB on average, and generated a clearer myocardial boundary distinction. Furthermore, the speckles were preserved according to the quality index based on local variance, the structural similarity index method, and normalized cross correlation values, being 0.82, 0.92, and 0.95 on average, respectively. Global longitudinal strain measurements on NF clutter reduced images were improved or equivalent compared to the original acquisitions, with an average increase in strain signal-to-noise ratio of 34%.

Index Terms—3-D, artifact reduction, clutter, clutter reduction, echocardiography, filter, image quality, medical ultrasound (US), speckle, strain imaging, wavelet transform.

I. INTRODUCTION

FOR the visualization of the heart, ultrasound (US) is generally the modality of choice due to its high temporal and spatial resolution, availability, and patient safety. However, US images are prone to artifacts (e.g., reverberation and aberration), leading to a significant reduction in image quality. Consequently, the distinction between the myocardium and the blood-pool is sometimes partly or completely faded. The introduction of harmonic imaging reduced these artifacts considerably due to depressed side and grating lobe levels. Additionally, the harmonic energy amplifies increasingly, inducing a weakened manifestation of multipath reverberations and near-field (NF) artifacts. In the literature, harmonic imaging has shown to reduce insufficient left ventricle visualization and inaccurate diagnostics in 2-D transthoracic echocardiography examinations from 38%–51% to 10%–24% [1]–[3]. However, in the remaining 10%–24% 2-D echocardiographic images, NF clutter remains a problem, leading to the inability to perform edge detection and segmentation. Additionally, NF clutter results in strain measurement errors [4]. Accordingly, correct functional diagnosis is hampered both visually and quantitatively.

NF clutter is created by multipath acoustic wave reverberations, aberrations, and/or of off-axis sidelobes detecting these reflected signals. In echocardiography, NF clutter is depicted as a white diffuse haze (Fig. 1). The multipath reverberation signal responsible for the NF clutter creation is attenuated with distance traveled, thus the clutter is predominantly present in the NF [5]. The exact origin of the multipath reverberation and aberration artifacts leading to NF clutter is still largely unknown. However, Fatemi *et al.* [6] performed a systematic study on possible NF clutter generation mechanisms in transthoracic cardiac images. According to their study, NF clutter generated by reverberation artifacts are produced either by a thick layer of fat, skin, and muscle, multiple reflections between lung and soft tissue, reverberations between air-filled cavities, and/or the position and orientation of the ribs with respect to the transducer, causing part of the US beam to deflect toward the lungs, subcutaneous fat or out-of-plane situated cardiac tissue. Hence, the level of NF clutter is dependent on the distance between the ribs, thorax size, lung size, chest fat layer thickness, and heart position within the

thorax [6]. NF clutter can either be stationary or in motion, depending on the movement of the reflective surface inducing the artifact (e.g., heart, lung, skin, and bone), the transducer, and the subject imaged [7].

Besides harmonic imaging, current clinical options to reduce the impact of NF clutter on US image contrast include contrast agents, which enhance the myocardium-blood-pool boundaries. However, contrast agents require invasive administration, longer examination procedures, and higher costs. Another clinical option, transesophageal echocardiography, is much less vulnerable to NF clutter, since the imaged and neighboring tissue primarily consists of smooth muscle and stratified squamous epithelium cells [8], [9]. Despite its capability to produce high resolution (3-D) images, transesophageal echocardiography is a semi-invasive exam, inducing patient discomfort, is not without risk, and demands extra medical personnel [10].

Alternatively, postprocessing algorithms have been developed for both NF clutter and general US noise reduction in echocardiography. General noise reduction methods are typically targeted at US speckle reduction [11]–[13], yet speckles are a necessitate for functional measurements, such as strain imaging. In stationary NF clutter reduction methods [5], the nonstationary NF clutter is unaffected, whereas akinetic myocardial regions are discarded by the algorithm. Furthermore, some algorithms adopt probabilistic methods for motion analysis of pixels [14]. These models perform well in healthy volunteers, though the abnormal motion dynamics in diseased hearts pose problems for these statistical models. The current state-of-the-art methods project the cardiac US data onto adaptively trained bases using either principal component analysis (PCA), singular value decomposition (SVD) [15], or morphological component analysis [16] for signal separation into an NF clutter and a cardiac tissue dictionary matrix, discarding the NF clutter matrices in the filtering process. However, these methods rely on a difference in motion characteristics between the NF clutter and cardiac tissue in the signal separation process. Hence, in case the tissue and clutter motion characteristics are similar, the algorithm will be incapable of distinguishing them (e.g., akinetic myocardial regions or tissue at end-diastole from static clutter, or clutter originating from cardiac tissue reflections with an identical motion frequency as the cardiac tissue). In addition, the pixel intensities in regions displaying cardiac tissue free of NF clutter can also be mitigated by these algorithms [15], [16]. Besides these temporal-based decomposition methods, some PCA decomposition or SVD-based methods also take into account the spatial information by transforming a 3-D stack of images with two spatial dimensions and one temporal dimension into one spatiotemporal representation, with all pixels from one frame arranged in one column and all time points for one pixel organized in one row, prior to the SVD decomposition [17]. However, this method has not been validated in echocardiography, so its performance on NF clutter is unknown. Furthermore, the NF clutter reduction PCA, SVD, and morphological component analysis methods are validated and perform best on IQ complex US data, and require sufficiently high frame rates to be able to distinguish
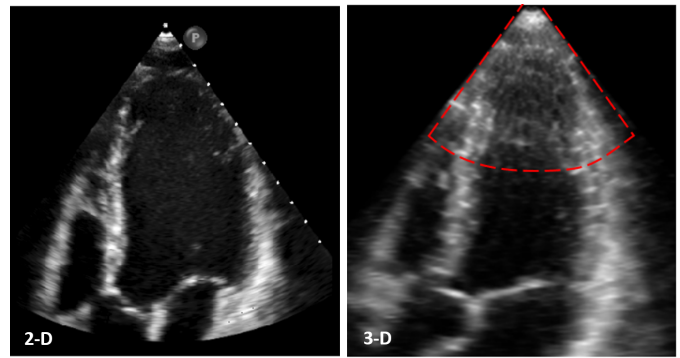

Fig. 1. Transthoracic echoes displaying the increase in NF clutter artifacts in 3-D US with respect to 2-D acquisitions. (a) 2-D image obtained in an apical window. (b) 2-D slice of a similar view acquired within the same subject using 3-D US. The NF clutter region is enclosed by a red-dotted line.

between the temporal characteristics of the artifact and tissue. Another state-of-the-art method uses soft wavelet thresholding to discard the estimated reflectivity values of the artifact in the clutter affected regions [18]. This method requires RF data, since the method exploits the high axial resolution and a relatively large dynamic range of the RF data. However, bright anatomical reflections are also mitigated by this soft thresholding method [18].

Most of the filters previously mentioned separate the US signal by linear decomposition, in which the NF clutter and tissue signal are divided along distinct bases. For the signal separation process they either employ adaptively learned or *a priori* determined bases to project the US data on. Although adaptively learned bases conventionally outperform methods based on *a priori* established approaches [16], [19], adaptive methods also have their limitations as previously identified. Techniques exploiting *a priori* defined bases could overcome the motion-related issues of the adaptive methods by filtering the NF clutter in the spatial frequency domain. However, the method should be able to distinguish the tissue speckle from the NF clutter, since US speckle is required for strain imaging.

The aim of this study is the implementation of an NF clutter reduction algorithm, which is able to filter NF clutter regardless of its motion characteristics (motion-invariance), preserves tissue speckle to support strain imaging, and is widely clinically applicable (i.e., good performance on conventional B-mode images).

The algorithm proposed analyzes each frame separately, and reduces NF clutter using oriented, complex wavelets, which decomposes the images into various oriented, frequency subbands. The NF clutter was expected to be present in both the lowest and highest bandpass subbands, since the NF clutter consists of a white haze covered in small white spots (Fig. 1). Moreover, tissue speckles are predominantly oriented in the lateral direction, and increase in width with depth, due to the reduction in line density and the increase in beamwidth of the phased array [20], [21]. Accordingly, the tissue speckles were absent in the highest frequency subband containing the
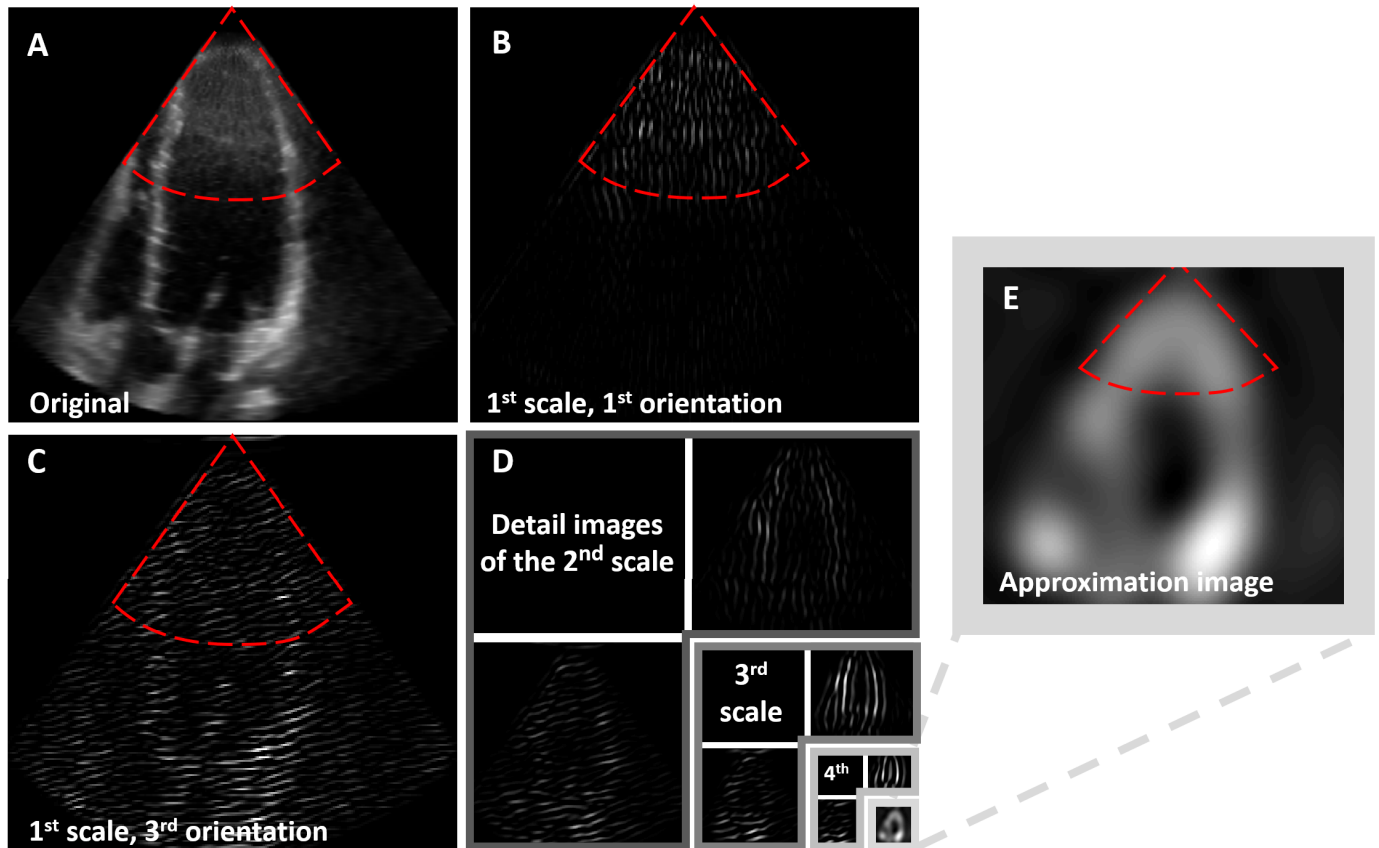
Fig. 2. Multiscale pyramid of an apical view image. (a) Slice of a 3-D trans-thoracic apical window volume in which the wedge-shaped NF clutter region is enclosed by a red-dotted line. (b) Detail image of scale 1 orientation 1, which corresponds to the smallest wavelet with a vertical orientation (0 π). This detail image contains primarily NF clutter specks and some vertically oriented myocardial structures. (c) Detail image of scale 1 orientation 3. This image shows horizontally oriented US speckles and NF clutter specks. (d) Detail images of scales 2–4 with orientation 1 and 3. The approximation is illustrated at the right bottom of the image, and is enlarged in (e). NF clutter is only visible in the first scale and in the approximation image. Accordingly, detail image (b) can be employed for the detection of the area containing NF clutter, whereas the detail images from (d) can be used to preserve the myocardial structures whilst discarding the NF clutter from the first scale and approximation image. For clarity, only the detail images with orientation 1 and 3 are shown.

axially oriented structures, whereas the NF clutter was visible in this specific subband. This observation led to the detection of the NF clutter region of the individual frame, which was used for filtering both the highest and lowest bandpass subbands. The algorithm abstains from filtering the myocardial regions, since NF clutter reduction in B-mode images leads to tissue speckle reduction or distortion of the myocardium, impeding functional measurements such as speckle tracking. In addition, the algorithm introduced only filters the NF clutter disturbed area, preserving image regions where NF clutter is absent.

The filter proposed is explained in more detail in Section II. The performance of this method is described in Section III. The performance is assessed on 3-D B-mode image planes of the heart, since it was observed in this study that 3-D acquisitions suffer to a greater extent from NF clutter (Figs. 1 and 8, which is included in the Multimedia files). The filter will be validated in a volunteer study, and in a clinical study, since anomalies in the heart rhythm, (regional) contraction velocities, respiration frequency, or heart shape might influence the performance of the filter proposed. In addition, the performance of strain imaging pre- and post-processing

will be compared. Finally, the proposed method will be compared to the spatiotemporal SVD filter. In contrast to the other state-of-the-art-methods, yet similar to the method proposed, the spatiotemporal SVD filter also considers distinctions in the spatial features of the clutter and tissue and is applicable to 3-D DICOM data [22], [23].

II. NF CLUTTER REDUCTION ALGORITHM

A. Image Decomposition

For the automatic detection of NF clutter a complex, oriented fast wavelet transform [24] was used for the decomposition of the US images into a multiscaled pyramid (Fig. 2). In this transform, wavelets were employed as modulated bandpass filters to extract frequency subbands from the images to obtain the so-called detail images (Fig. 2(b)–(d)). The family of wavelet functions applied here consisted of translated, dilated, and/or contracted variants of the wavelet function

$$\psi_{s,p}(x) = \frac{1}{\sqrt{s}} \psi\left(\frac{x-p}{s}\right) = \frac{1}{\sqrt{s}} \phi\left(\frac{x-p}{s}\right) e^{j\omega_c\left(\frac{x-p}{s}\right)} \quad (1)$$

where s is the scaling factor regulating the width of the wavelet and p the translation factor manipulating its position [25],

$\phi(x)$ a Gaussian lowpass filter, x the spatial positions, and ω_c the center frequency of the wavelet ψ.

The fast wavelet transform is an iterative process in which every step was started by the application of a lowpass filter, creating the so-called approximation image. Subsequently, the approximation image was filtered using a highpass filter, constructing a scale of detail images. Hence, each scale containing detail images represents the highest remaining part of the frequency spectrum after the lowpass filter operation. For computational time reduction, after each step, the approximation image was downsampled by a factor of 2. In this method, the images were decomposed into four scales [Fig. 2(b)–(d)] and an approximation image [Fig. 2(e)]. The complex variant of the wavelet transform was used, since most structural information is embedded in the phase of a signal [26]. For the filter, either a 2-D or 3-D complex, oriented fast wavelet transform was applied, depending on whether an image plane, frame, or volume was filtered.

An oriented fast wavelet transform was adopted, in which directional derivatives were used to obtain oriented detail images. The orientations ranged from 0 to $((k-1)/k)\pi$ rad in steps of (π/k) with (k) the total number of orientations, being four in this method. For computational efficiency, k was kept as small as possible. The directional derivatives formed a steerable basis, meaning they were rotated copies of each other, and they were all linear combinations of the base functions [24]. In order to prevent aliasing and to introduce shift-invariance, the total wavelet transform contains an overcomplete representation, due to not performing subsampling of the oriented detail images. The steerable pyramid is overcomplete by a factor $(4k)/3$ [24].

US speckles are generally oriented in the lateral direction, since the lateral resolution of a phases array declines with depth, due to the reduction in line density and the increase in beamwidth of the phased array [20], [21]. Consequently, in images without the sector tilt function employed, tissue speckle is absent in the first scale with orientation 0 rad, whereas the NF clutter is present in this detail image [Fig. 2(b)]. Consequently, this detail image is used for the detection of the NF clutter region. In images with the sector tilt function applied, either rotation of the US image should be performed prior to the application of the filter, or a different oriented detail image should be chosen corresponding to the tilt of the US image.

B. NF Clutter Manifested Region Detection

As can be observed in Fig. 2(b), the detail image in the first scale at orientation 1 (at 0 rad), predominantly contains NF clutter. Accordingly, this detail image is used to automatically select the area encompassing the NF clutter. First, a threshold was applied with a cutoff value of 5% of the maximum value of this detail image. This threshold was visually, empirically determined for optimal performance in this specific application. In case this approach is applied in a different application, this threshold has to be readjusted just once. Subsequently, a closing procedure was performed to obtain a continuous NF clutter region.

The clutter artifact attenuates with depth. Hence, it is only present in the NF. Furthermore, the NF clutter region is wedge-shaped, since a phased array was used during imaging. Therefore, for computational efficiency, the oriented detail image (scale 1, orientation 1) was projected onto polar coordinates, after the application of the threshold. In the newly formed polar image, the previously wedge-shaped clutter area was transformed into a rectangle. This rectangular NF clutter region was selected, which ended at image rows containing less than 50% nonzero pixels. This value of 50% does not have to be defined very precisely, since the distal edge of the NF clutter area is relatively sharp. Everything outside this rectangle was discarded. The resulting NF clutter region mask was transformed back to Cartesian coordinates, to obtain a wedge-shaped NF clutter mask.

However, this NF clutter mask also contained cardiac tissue areas, which had to be removed from the mask. This was achieved by subtracting all oriented detail images from scales two until four from the NF clutter mask M, since these levels captured structures in the range from approximately 2 to 22 mm, which includes the myocardium thickness

$$M := M - T\left[\sum_{i=2}^{n}\sum_{j=1}^{m} s_{i,j}\right] \tag{2}$$

with $s_{i,j}$ the detail image of scale i and orientation j, and n and m the total number of scales and orientations, respectively, both equaling to four. Prior to subtraction, a threshold T was applied to the fused detail images. In this thresholding method, the pixels were divided into two groups, being myocardial tissue and other, for which parameter η is minimized [27]. Here, η is defined as

$$\eta = \frac{\sigma_B^2}{\sigma_G^2} \tag{3}$$

with σ_G^2 the global variance of the fused image and σ_B^2 the variance between the myocardial tissue group and other group defined as

$$\sigma_B^2 = \sum P_i(m_i - m_G)^2 \tag{4}$$

with P_i the probability of group i occurring, m_i the average pixel intensity in group i, and m_G the average intensity of the fused detail images.

C. NF Clutter Reduction

The NF clutter was mitigated in all oriented detail images of the first scale [Fig. 2(b) and (c)], and in the approximation image [Fig. 2(e)], since these contain the NF clutter.

In the detail images from the first scale, the NF clutter wavelet coefficients are discarded in all orientations (j), using

$$s_{1,j} := s_{1,j} - |M - 1|. \tag{5}$$

Subsequently, in the approximation image, the NF clutter region was replaced by a downsampled fusion of all oriented detail images of scales two until four A_{new}

$$A_{\text{new}} = D_2\left[M\sum_{i=2}^{n}\sum_{j=1}^{m} s_{i,j}\right] \tag{6}$$

with D_2 2-D downsampling by a factor 16. To keep similar magnitude values within this replaced region compared to the original approximation image (A_{old}), the downsampled NF clutter replacement area (A_{new}) was normalized and multiplied by the summation of the old approximation NF clutter region prior to replacement

$$A_{new} := \frac{\sum A_{old}}{\sum A_{new}} A_{new}. \tag{7}$$

However, the new approximation pixels were restricted in maximum intensity, since the new pixels cannot exceed those of the old ones. Otherwise, artifacts would appear in the image.

Finally, the image is reconstructed using the inverse fast wavelet transform, obtaining the NF clutter reduced images. This was achieved by convolution of the filtered detail images and the approximation image with the corresponding basis functions (and of course upsampling). The transform is self-inverting, which implies that the product of the basis and projection functions yields the identity matrix [24].

III. *In Vivo* VALIDATION

A. Acquisitions

1) Volunteer Study: Ten healthy volunteers were recruited for *in vivo* validation of the NF clutter reduction algorithm. The volunteers, eight males and two females, were all in the age of 21–30 years. The inclusion criteria included no current or past heart ailments. The local Medical Ethics Committee of the Catharina Hospital, Eindhoven, The Netherlands, reviewed the protocol and granted ethical approval. All participants gave written consent.

The subjects were positioned in a left lateral decubitus position. 3-D apical and parasternal volumes were acquired using a matrix phased array (X5-1) transducer with a frequency range of 1–5 MHz, connected to a Philips Epiq machine (Philips Healthcare, The Netherlands). The harmonics acquisition mode was used whilst the images were obtained real-time with a frame rate of 20 Hz for seven heart beats. The US data were transferred to an external computer in DICOM format, where the images were filtered (see Section II) and analyzed using algorithms implemented in MATLAB (MATLAB 2018b, MathWorks, Natick, MA, USA).

2) Clinical Study: A retrospective study was performed on 20 patients with different indications for echocardiographic examination, consisting of: 1) valvular heart disease; 2) coronary artery disease; 3) hypertensive cardiomyopathy; 4) chest pain assessment; 5) heart rhythm disorder; and 6) cardiac sarcoidosis. 2-D images of the apical four-chamber and parasternal long-axis view were obtained using the same probe and US apparatus. Furthermore, 3-D apical volumes were acquired in similar positions as the 2-D apical images. One or two heart beats were obtained using harmonic acquisition mode, exported in DICOM format, and filtered and analyzed in MATLAB.

B. Performance Evaluation of the Filter Proposed

The performance of the NF clutter reduction filter was analyzed based on the improvement in image quality, the degree of US speckle preservation, and its effect on speckle tracking-based 2-D strain imaging, described in Sections III-B1–III-B3.

1) Image Quality Improvement: Image quality improvement induced by the NF clutter reduction algorithm was quantified using the change in contrast-to-noise ratio (CNR) (ΔCNR) and signal-to-noise ratio (SNR) (ΔSNR). The calculations were performed on the upper half of the middle slice planes of the 3-D apical and parasternal volumes, since those are the NF clutter manifested regions. The change in image contrast pre and post NF clutter reduction was calculated using the CNR

$$CNR = \frac{\mu_M - \mu_B}{\sigma_B} \tag{8}$$

with μ_M and μ_B the average signal intensities of the myocardium and the blood-pool, respectively, and σ_B the standard deviation of the blood-pool. The standard deviation of the myocardium was not taken into account in the equation. A drop in this standard deviation would falsely suggest image enhancement, though it actually implies an unwanted reduction in US speckles.

2) Speckle Preservation Assessment: US speckle preservation was assessed using three metrics. First of all, the local variances in the myocardium between the original image and the NF clutter reduced image were correlated using the quality index based on local variance (QILV), which is based on the mean and standard deviation of the local variance, and spatial coherence [28]. Second, the mean correlation in terms of local (structural) statistics in the heart wall after NF clutter reduction was evaluated using the structural similarity index method (SSIM), which compares the images based on contrast, luminance, and structure [29]. Third, US speckle alteration was analyzed using normalized cross correlation (NCC), which compares normalized local intensities in the myocardium [30].

For all metrics, a value of 1 is obtained provided the original and NF clutter filtered myocardial regions are identical. Solely the image regions depicting myocardial tissue were considered.

3) Strain Imaging: Global longitudinal strain was calculated in the apical data sets, since it was aligned with the axial direction of the US, which is the axis with the highest spatial resolution. Moreover, global longitudinal strain is a widely used diagnostic parameter in the clinic [31]–[34].

For speckle tracking, a coarse-to-fine block-matching algorithm was used [35]. The block-matching algorithm used NCC with tracking kernel window sizes of 18.1 mm $\times$ 17.8 mm in the first step, and 9.4 mm $\times$ 9.3 mm in the refined step. The tracking kernel windows had an overlap of 73% and 38%, respectively. Subsequently, the computed displacements were filtered using a 3 $\times$ 3 pixel spatial median filter to remove outliers.

The possible enhancement in strain computation due to the NF clutter reduction filter was quantified using strain ΔSNR, defined as

$$\Delta SNR = \frac{-\mu_R}{\sigma_R} - \frac{-\mu_O}{\sigma_O}. \tag{9}$$

With μ the mean of the global longitudinal strain curve of the original image (O) or NF clutter reduced image (R), and
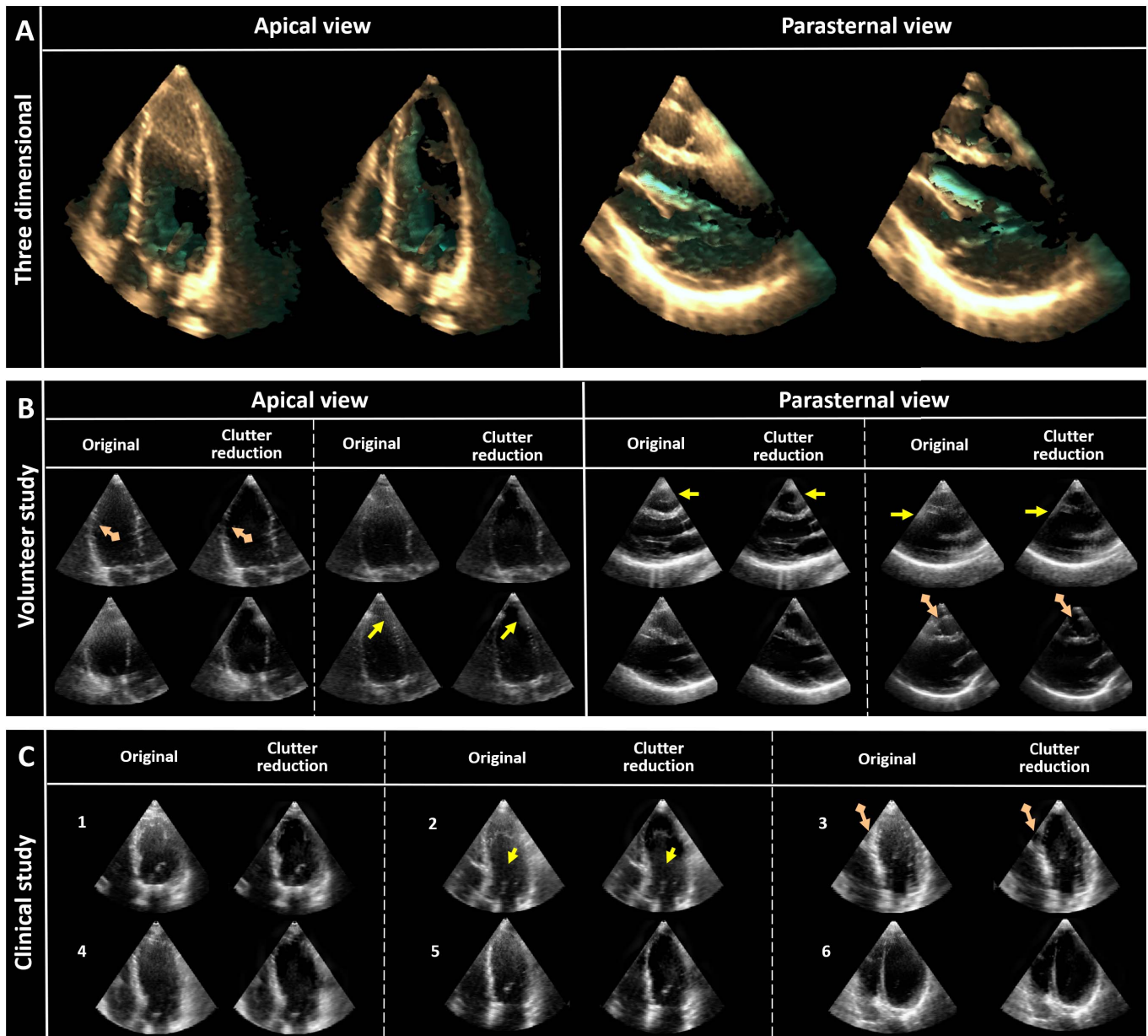
Fig. 3. Representative images showing the results of the NF clutter reduction algorithm applied to (a) 3-D apical and parasternal volume, and 3-D images of (b) volunteer and (c) clinical acquisitions at end-diastole. (a) For clarity, only the middle section of the 3-D volume is shown. (b) and (c) Yellow arrows indicate regions where NF clutter elimination was incomplete. The orange arrows with the diamond-shaped ends point out regions where myocardial tissue was incorrectly removed or slightly reduced in intensity value. For every example, first the original image is shown, and to their right the NF clutter compressed result is depicted. Overall, almost all of the NF clutter was removed, whilst preserving the US speckles. (b) Four apical and four parasternal representative examples are shown. An overview of all acquisitions is shown in Fig. 9 included in the multimedia files. (c) For each of the included indications for echocardiography in this study, a representative example is shown. The indications were: 1) valvular heart disease; 2) coronary artery disease; 3) hypertensive cardiomyopathy; 4) chest pain assessment; 5) heart rhythm disorder; and 6) cardiac sarcoidosis. In Fig. 10 included in the multimedia files, the results of all acquisitions can be found.

σ the corresponding temporal average of the spatial standard deviations of the frames of the cardiac cycle.

4) Comparison to State-of-the-Art: The filter proposed was compared to state-of-the-art spatiotemporal SVD algorithm [17], which considers both the temporal and spatial differences between the clutter and tissue. In this approach, the stack of 2-D frames over time was transformed to a Casorati matrix where the first dimension is space and the second is time. Subsequently, the Casorati matrix is decomposed into a spatial singular vector matrix (U), a temporal singular vector matrix (V), and a diagonal matrix containing the singular values (S) ordered from biggest to smallest. The matrices U and V are orthonormal. The largest singular values represent the structures with the relatively highest coherency in space and time (i.e., tissue signal), whereas the smallest values symbolize the less coherent features (i.e., NF clutter and noise). Accordingly, the biggest $n-1$ singular values were preserved, thus discarding all smaller singular values representing the NF
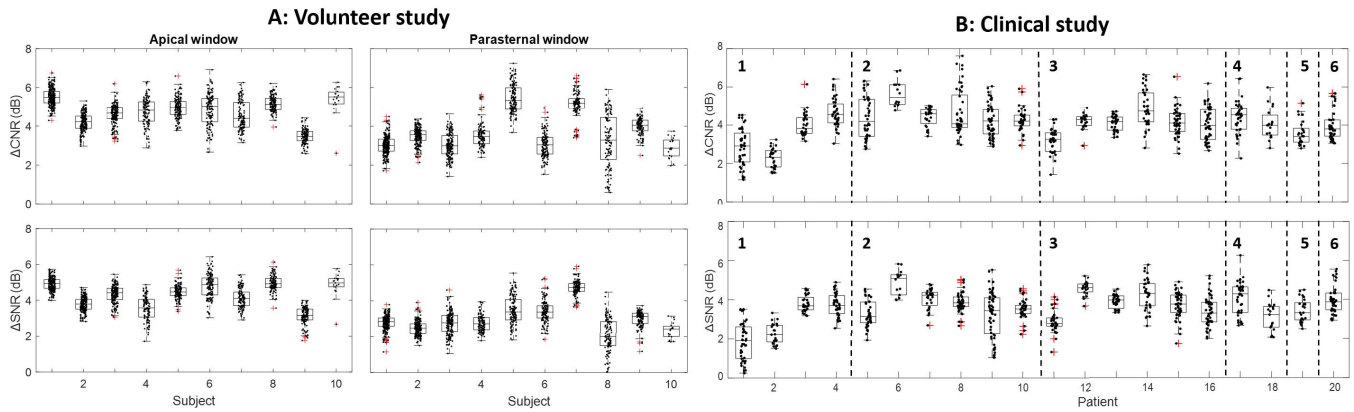
Fig. 4. Image quality metrics calculated in the NF clutter affected regions in the (a) volunteer and (b) clinical acquisitions. For both, differences in CNR and SNR were computed, comparing the original image to its NF clutter mitigated counterpart. Each dot represents the metric value of a specific time frame. (a) Left subfigures: image quality metrics observed in the apical window. Right subfigures: parasternal window results. (b) Change in CNR and SNR of the 3-D apical view from the clinical data sets with different indications for echocardiographic exam: 1) valvular heart disease; 2) coronary artery disease; 3) hypertensive cardiomyopathy; 4) chest pain assessment; 5) heart rhythm disorder; and 6) cardiac sarcoidosis. The increases in CNR and SNR were consistent for the different indications, and were comparable to the data sets from the volunteer study.

clutter and noise. The threshold value n was varied between 2 and 20 to examine the effect of the spatiotemporal filter and the choice of the singular value threshold n in this application. After imposing the singular value threshold n, the NF clutter reduced image was reconstructed using

$$I = USV^*　\qquad (10)$$

with $*$ the conjugate transpose.

C. Results

In the clinical study, one in five 2-D acquisitions were affected by NF clutter, whereas in four out of five 3-D data sets the artifact was observed (Fig. 8 included in the multimedia files). Accordingly, the 3-D data sets were analyzed.

1) Volunteer Study: The NF clutter reduction algorithm was applied successfully to all data sets. Two representative examples of NF clutter reduced 3-D echocardiography volumes at end-diastole are shown in Fig. 3(a). An improved visual contrast can be observed in the NF clutter filtered volumes. In addition, the myocardial-blood-pool borders show enhanced visual delineation. Subsequently, the NF clutter reduction resulted in an unobstructed view of the myocardium situated deeper into the 3-D volume.

Fig. 3(b) shows representative example results of the NF clutter reduction algorithm in 2-D volume plane slices obtained at the first end-diastolic moment. This figure is used to present the visual performance of the NF clutter reduction filter. The NF clutter was eliminated almost completely in all images (the remaining NF clutter is indicated by the yellow arrows). Furthermore, the myocardial US speckles appear to be preserved in all cases. Additionally, the image regions without NF clutter were successfully undisturbed by the algorithm. However, in some cases, minor pieces of the myocardium were discarded or slightly dimmed (pinpointed by the orange arrows with the diamond-shaped ends). The results of all volunteers are shown in Fig. 9 in the multimedia files available at http://ieeexplore.ieee.org.

In all subjects, image quality improvement was assessed using ΔCNR and ΔSNR values, which are displayed in Fig. 4(a) for the apical and parasternal volumes. Consistent increases are observed in both the ΔCNR, 4.8 $\pm$ 0.8 and 3.8 $\pm$ 1.1 dB, and ΔSNR, 4.3 $\pm$ 0.8 and 3.0 $\pm$ 0.9 dB, for the apical and parasternal volumes, respectively, on average. All frames have a positive Δ SNR and CNR.

Strain imaging requires the presence of US speckles in the myocardium. Hence, speckle conservation was quantified using the QILV, SSIM, and NCC metrics [Fig. 5(a)]. The mean calculated QILVs for the apical and parasternal were 0.75 $\pm$ 0.02 and 0.85 $\pm$ 0.04, respectively. The SSIM was computed to be 0.93 $\pm$ 0.004 and 0.94 $\pm$ 0.01, respectively. Finally, the average NCC values were 0.96 $\pm$ 0.01 and 0.97 $\pm$ 0.01 for the apical and parasternal volumes, respectively.

Strain computation performance evaluation, pre- and post-processing, was executed by assessing the global longitudinal strain curves acquired from the original and NF clutter filtered images. Fig. 6(a) displays one of the longitudinal strain tracking results for an apical image and for its NF clutter reduced counterpart, over one cardiac cycle starting at end-diastole. Fig. 6(b) exhibits the end-systolic strain field corresponding to the pre- and post-NF clutter reduced strain curves, respectively, which were shown in Fig. 6(a). The end-systolic strain fields present similar strain results.

Fig. 6(a) and (c)–(g) shows improved global longitudinal strain curves, as confirmed quantitatively by the strain ΔSNR values shown at the left bottom of these subfigures. These data sets display similar or slightly improved mean strain values accompanied with smaller standard deviations. The standard deviation ranges of the NF clutter reduced images are all within the range of their complementing nonfiltered data set. Fig. 6(h) shows a reduced strain ΔSNR, which is evoked by the augmented standard deviations. The strain measurements of the NF clutter reduced images shown in Fig. 6(i)–(k) are similar to their original counterparts, as demonstrated in the
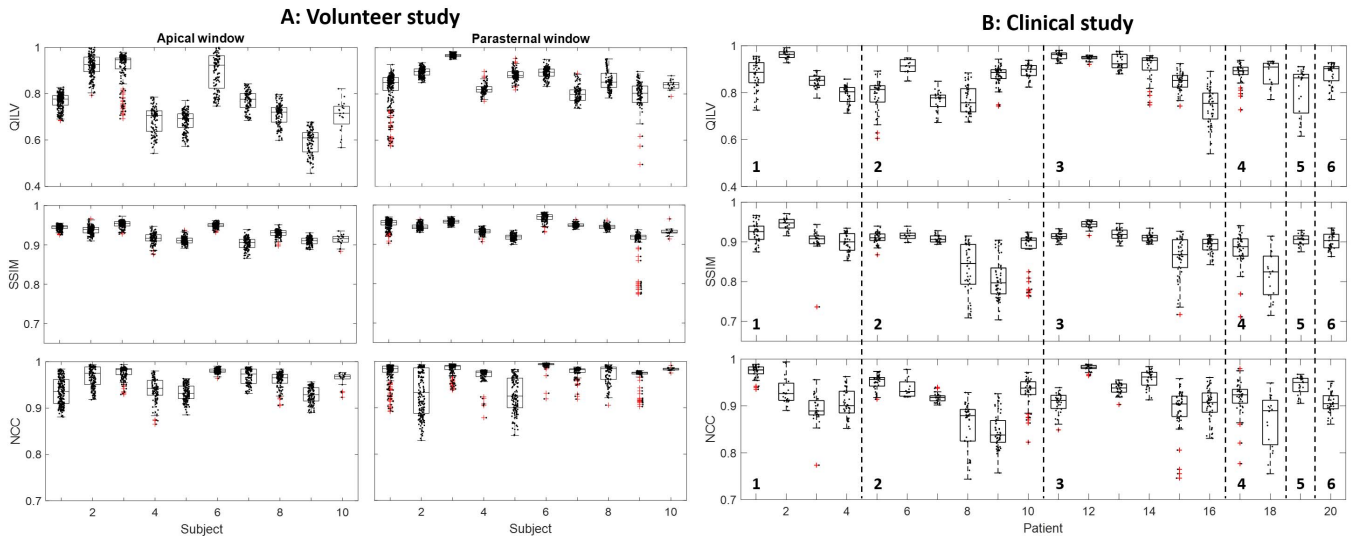
Fig. 5. Myocardial speckle preservation quantification metrics (i.e., QILV, SSIM, and NCC), correlating the original frames with the NF clutter mitigated equivalents. QILV is predominantly sensitive to blurring, SSIM is primarily susceptible for noise (e.g., US speckle), and NCC is a normalized pixel-to-pixel comparison. For all metrics, a value of 1 is obtained in case the original and filtered image are identical. Each dot represents a specific time frame within the acquisition. (a) Volunteer study, showing the speckle preservation quantification metrics of the apical window in the subfigures on the left, and those of the parasternal window on the right. (b) Quantification metrics of the clinical study obtained in the apical window. All measured values are in close proximity of 1.

mean strain values, standard deviations, and ΔSNR strain values.

The method proposed was compared to a state-of-the-art spatiotemporal SVD filter. The average singular values for the apical and parasternal data sets ordered from big to small are shown in Fig. 7(a). For singular value thresholding, the threshold value n was varied between 2 and 20, for which only the biggest $n-1$ singular values were preserved. Each dot in Fig. 7(b) represents the temporally averaged ΔCNR values of the volunteers for a value n. The maximum average increase in CNR is approximately 0.5 dB, though the surplus of the ΔCNR values are negative. A reduction in n leads to a reduction in ΔCNR [Fig. 7(b)]. In addition, the decline in n is associated with an increased elimination of relatively small and fast-moving structures [Fig. 7(c)], inducing the progression of blurriness in the resulting image. In contrast to the method proposed, the white haze of the NF clutter remains present for all chosen values of n.

2) Clinical Study: Again, the filter was successful in all 3-D acquisitions, regardless of the patient's indication. Fig. 7(c) displays representative example results of the NF clutter reduced middle volume plane slices acquired at the first end-diastolic moment. The results of all 3-D acquisitions are shown in Fig. 10 in the multimedia files available at http://ieeexplore.ieee.org. The filter has a similar effect on the patient data in comparison to the volunteer data; in all patients the NF clutter was almost fully discarded, the myocardial speckles seem to be preserved, image areas showing no NF clutter were unaffected, and in few images, small segments of the myocardium were slightly dimmed or discarded.

For all patients, the ΔCNR and ΔSNR values are displayed in Fig. 4(b) for the 3-D apical volumes, ordered by indication. Coherent enhancements in both the ΔCNR and ΔSNR were

noticed for all indications (4.1 $\pm$ 1.0 and 3.5 $\pm$ 0.9 dB on average, respectively), which were comparable to the volunteer data sets. For every frame, Δ SNR and CNR were positive.

Fig. 5(b) shows the QILV, SSIM, and NCC values (with the average values being 0.86 $\pm$ 0.08, 0.89 $\pm$ 0.05, and 0.91 $\pm$ 0.05, respectively). All values are close to 1 and the results are consistent for all patients.

IV. DISCUSSION

Despite the adoption of harmonic imaging, one in five 2-D transthoracic images of the clinical study were affected by NF clutter, which is comparable to literature were 10%–24% of the exams were reported to be insufficient for diagnostic purposes as a result of the artifact [1]–[3]. 3-D echocardiography was more severely affected by NF clutter (four out of five), which is unfortunate, since 3-D echocardiography is capable to fully capture the complex contraction shape and geometry of the heart. Additionally, in contrast to 2-D imaging, 3-D echocardiography is less susceptible to diagnostic variability, since it is unaffected by out-of-plane shifts and does not require a specific selection of the imaging plane [36].

Therefore, in this study, a new NF clutter reduction algorithm for echocardiography has been introduced, applicable for both 2-D and 3-D echocardiography. The NF clutter was filtered based on its visible spatial frequency characteristics observed using a complex oriented fast wavelet transform. The principal advances of the algorithm proposed include the following.

1) It disregards temporal information. Hence, the algorithm is cardiac, respiratory, transducer, and patient motion-invariant.
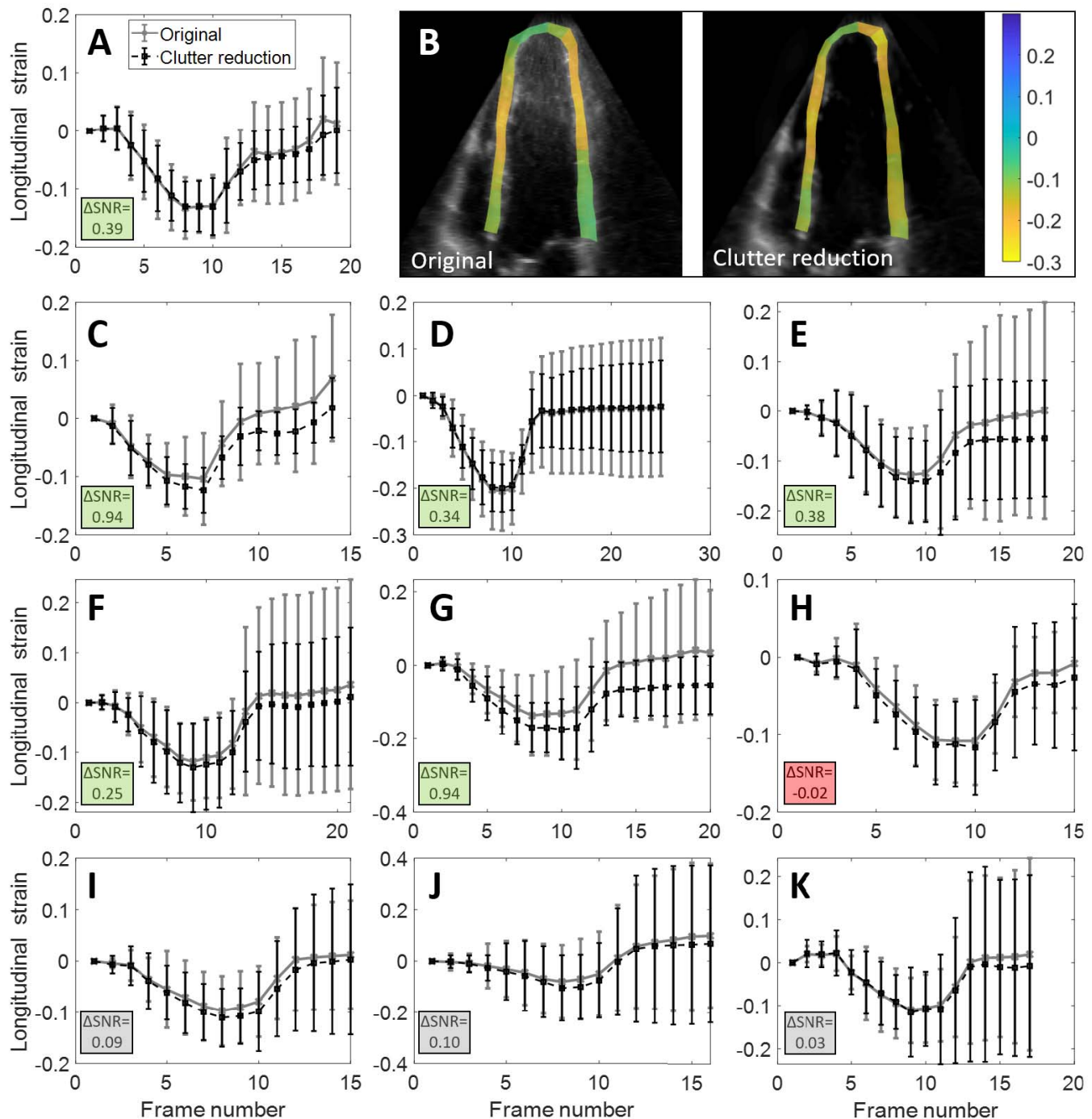
Fig. 6. Global longitudinal strain curves of the original and NF clutter reduced images, acquired through speckle tracking. (a) Global longitudinal strain computed over a cardiac cycle of the original data set and its NF clutter diminished complement. (b) Calculated longitudinal strain field at end-systole of (left) an unfiltered apical volume slice plane and of (right) the NF clutter reduced image. (c)–(g) Global longitudinal strain curves showing an improvement in strain computations post NF clutter reduction. (h) Declined NF clutter reduced strain measurement. (i)–(k) Similar strain curves for the original image compared to its NF clutter reduced counterpart. Left bottom of the subfigures: change in the strain SNR (ΔSNR).

2) It only filters the image regions containing NF clutter.
3) The preservation of US speckles is achieved, resulting in step 4.
4) Improved or comparable strain imaging results. The filter proposed was validated in both a volunteer study and in a small clinical study.

All 3-D data sets in the volunteer study contained some degree of NF clutter, whereas in the clinical study, four out of five acquisitions contained the artifact. Hence, the number of 3-D data sets in this study containing NF clutter was four times as high in comparison to 2-D data sets obtained in a similar position. Literature lacks information on the
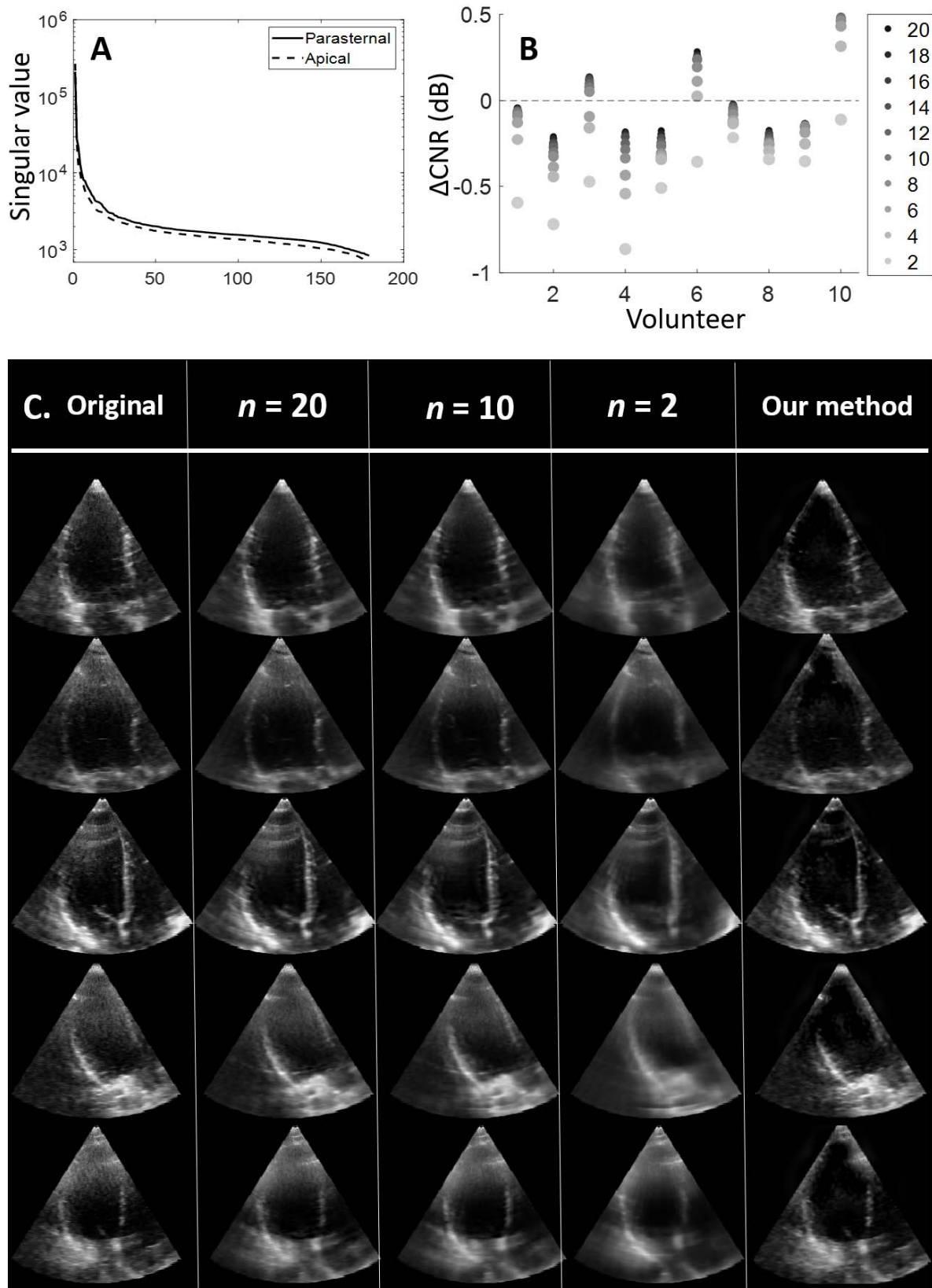
Fig. 7. Comparison to a state-of-the-art spatio-temporal SVD filter. (a) Average singular values of the matrix *S* ordered from biggest to smallest for the apical and parasternal data sets. (b) Changes in CNR values after application of the SVD filter. For each volunteer, the average ΔCNR is computed for different values of the singular value threshold *n*. The ΔCNR becomes smaller with a reduction in *n*, thus with discarding less information. (c) Examples of the effect of the SVD filter on the 3-D echocardiography images. With a decline in *n*, an increase in elimination of small structures (e.g., NF clutter particles, US speckle) can be observed, resulting in the blurring of the images. In contrast to the proposed method, the white NF clutter haze still remains visible.

prevalence of NF clutter in 3-D echocardiography. Hence, the reason for the higher prevalence of NF clutter in the 3-D acquisitions is unknown. It is hypothesized that 3-D US is more sensitive to NF clutter, due to the wider acoustic beams, or use of a 2-D aperture for both lateral and elevational focusing (resulting in augmented reverberation and aberration artifacts), a difference in acquisition scheme, the beamforming algorithm, or a combination of the previous.

The NF clutter was reduced in all 3-D data sets, whilst preserving all or most of the tissue. Accordingly, the visual contrast was enhanced, leading to easier, clearer, and faster myocardial boundary delineation. In 3-D volume rendering, the cleared NF exposed the previously occluded myocardial wall sections. These observations were confirmed by the increases in CNR and SNR as a result of the NF clutter reduction filter. The ΔCNR and ΔSNR values demonstrated a consistent increase in both parameters for all data sets of both the volunteer and clinical study. The spread observed within each data set can be explained by variations in myocardial signal strength, NF clutter density, and/or NF clutter intensity during the cardiac cycle.

Speckles are a requirement not only for functional measurements, such as strain, but are also used by clinicians for visual myocardial wall velocity assessment. Generally, trained experts and clinicians prefer the speckled images, since speckle reduction induces a perceived decrease in image sharpness [37], [38]. Consequently, one of the aims of the proposed algorithm was US speckle preservation. This preservation was accomplished in this study according to the quantification metrics (QILV, SSIM, and NCC).

The QILV is particularly sensitive to blurring [28]. Yet, noise or global intensity changes within the analyzed region barely affect the QILV. In contrast, the SSIM is primarily influenced by white noise and global intensity alterations. Hence, the QILV and SSIM both have a different bias, thus are complementing each other in the US speckle preservation quantification task.

The SSIM and NCC parameters are close to one, inferring a general similarity in US speckles between the original and filtered images. Both metrics show consistent results in all data sets. The small decreases in these parameters might be caused by a small global intensity reduction or by local myocardial segment removal. In the parasternal view in subject 2 and 5, the big spread in NCC values is caused by a piece of the myocardium being removed in the filtering process in only a phase of the cardiac cycle.

The QILV metric has a high sensitivity for blurring: a convolution with a 5×5 pixel Gaussian kernel will depress the QILV value by approximately 0.5. Consequently, minor blurring-like deviations in the myocardium lead to relatively strong decreases in the QILV metric. In the volunteer study, the apical acquisitions displayed a bigger reduction in QILV values in comparison to the parasternal images. This difference in overall QILV value is caused by the relatively lower NF myocardial signal intensity in the apical images, due to the bigger angle between the myocardial tissue normal and the acoustic beam. In case the normal of the reflective surface is parallel to the acoustic beam direction, the US signal

intensity is maximal. In the NF, the lower signal intensity in the apical view leads to a poorer visual discrimination of the tissue from NF clutter artifacts. Consequently, the NF clutter reduction filter might slightly reduce the myocardial background intensity, leading to a decline in the QILV value. However, the QILV values of the clinical study were similar to the parasternal images of the volunteer study, due to the better image quality of the clinical acquisitions.

A demonstration was included to show the filter proposed has no negative effect on global longitudinal strain computation, meaning the US speckles were indeed preserved and no speckle-tracking image artifacts were introduced. The global longitudinal strain measurements post NF clutter reduction produced improved or equivalent results compared to the original images, with the exception of one data set. In this exception, more than 50% of the myocardial wall was invisible in the original acquisition. In few images, a piece of the myocardium was dimmed in intensity or removed. Consequently, US speckle tracking was slightly corrupted in these areas. In most measurements, the standard deviation of the displacement field was reduced, which was verified by the increase in strain SNR. Additionally, in some cases, the mean of the global longitudinal strain was also improved, since it was closer to zero at the end of the cardiac cycle, due to a reduction in NF clutter induced drift in the displacement fields. Furthermore, in some data sets, the mean strain at the end of the cardiac cycle was unequal to zero in the NF clutter reduced acquisitions, though in the original images the mean strain in fact returned to zero. In these cases, the myocardium is tracked correctly in the NF clutter reduced images. The measured residual strain is caused by the still slightly contracted myocardium (see multimedia files). Accordingly, the strain curves of the NF clutter reduced images display improved displacement tracking due to the artifact reduction.

The displacement tracking performance of other NF clutter reduction algorithms has been assessed by Mauldin *et al.* [16] in eight mice hearts. The filters improved myocardial tracking. However, the filters also corrupted regions without NF clutter present. The NF clutter reduction filter introduced in this study only filters the NF clutter containing areas of the image.

A big advantage of this approach for echocardiography is that it filters the images in the spatial frequency domain. Hence, it does not rely on significant motion differences between the NF clutter artifact and the cardiac tissue, which might be absent in, for example, infarcted regions, or during end-diastole. Mitigation of NF clutter is executed for each time frame individually, ergo the motion characteristics of the NF clutter and cardiac tissue are ignored. Consequently, the algorithm is able to reduce NF clutter originating from moving tissues (e.g., lung, cardiac tissue). Contrarily, the successful state-of-the-art NF clutter reduction methods exploiting adaptive filter coefficients, such as the PCA [15] and the single value filter [16], lose performance with transducer motion, the presence of non-static NF clutter, and in quasi-static imaged tissue (e.g., at end-diastole, infarcted myocardial regions). On the other hand, another state-of-the art SVD filter considers spatial coherence conjointly with the

temporal fluctuations. The spatiotemporal filter is currently used for clutter reduction in Doppler data [17] and to improve speckle tracking in the skeletal muscle system [22], [23]. In addition, a soft wavelet thresholding approach has been developed for clutter reduction, which eliminates the estimated artificial reflectivity values in the wavelet coefficients [18]. However, this soft thresholding method requires RF data containing a high axial resolution and large dynamic range. Accordingly, the method proposed was compared to the spatiotemporal SVD filter.

As described previously, the NF clutter is depicted as a diffuse white haze, with its spectral content encompassing both relatively high and low frequencies. After application of the spatiotemporal filter [17], a reduction in the high frequencies associated with the NF clutter is achieved when preserving only a few of the largest singular values. However, in case only the larger values are preserved, the relatively fast-moving structures are conjointly removed (i.e., US speckle and cardiac values). This mitigation of the relatively small, rapid structures implicates loss of detail, which amounts to blurring of the image. Moreover, the low frequencies of the NF clutter are condensed together with the myocardial tissue in the highest singular value, which is also the case in musculoskeletal data sets [22], [23]. Accordingly, elimination of the low frequency component of the NF clutter is impossible, unless the data sets contain a very high temporal and/or spatial resolution, which is currently not achievable in conventional 3-D echocardiography. Furthermore, the loss of detail combined with the failure to eliminate the low frequency portion of the NF clutter, results in the relatively low gain or even loss of image contrast, which is quantified by the generally negative ΔCNR values. Alternatively, the SVD filter construction could be performed using only the clutter affected region. This adapted SVD filter would prevent loss of information in the clutter-free areas. However, the relatively smaller image area included in this adapted SVD filter would lead to a reduction in spatial coherence differentiation, leading to a declined spatial sensitivity of the filter. Additionally, blurring of the clutter affected region would remain a problem, as would be the presence of the low frequency content of the NF clutter. Hence, in 3-D DICOM echocardiography, the method proposed outperforms state-of-the-art spatiotemporal filter.

Besides a validation in a volunteer study, a small retrospective clinical study has been performed to investigate the performance of the filter in daily clinical practice. The acquisitions included were all 3-D measurements obtained during the last six months, which had different indications for echocardiography (see Section III-A2).

As expected, motion-related anomalies in cardiac patients (e.g., heart rhythm and contraction velocity disorders due to coronary artery disease or cardiac sarcoidosis) had no impact on the performance of the filter proposed, since the algorithm presented ignores temporal information. Furthermore, the performance of the filter encountered no hinder from structural myocardial deformations (e.g., cardiomyopathy, alterations caused by valvular heart disease). These conclusions were drawn from the visual images results as shown in Figs. 3(c) and 10, which is included in the multimedia files, and the computed Δ CNR and SNR values, which were similar to those obtained in the volunteer study. Additionally, the tissue speckle was preserved, according to the QILV, SSIM, and NCC values, which were close to one. Hence, the filter proposed performed equally well in daily clinical practice as it would in healthy volunteers.

Moreover, the filter proposed is implied to be well suited for exercise stress echocardiography, in patients with a difficulty to perform breath hold, or with deviating breathing patterns, since it disregards temporal information, in contrast to the state-of-the art methods.

However, extreme structural deformations (e.g., severe cases of hypertrophic myopathy) might have an unforeseen effect on the filter, though this possible effect is outside the scope of this article. Additionally, NF clutter might be enhanced or exhibit different morphological properties in patients with very small spaces between the ribs or a very thick layer of adipose tissue on their chest.

Some NF clutter artifacts were still visible in the filtered images in case the artifact region was locally very dense. In these local dense regions, some NF clutter signal might be present in the detail images of scale two until four, since these dense regions have similar area dimensions as myocardial tissue. However, including these scales in the filtering process might induce an increase in myocardial tissue elimination.

In addition, in many parasternal images, there is still some NF clutter present at the image boundaries. The sharp change in pixel intensity at these borders might result in the presence of some NF clutter signal in the detail images of scales two until four. This might be solved by padding the image boundaries by slightly altered boundary patch copies, during the filtering process only.

Moreover, some myocardial wall segments are completely occluded by NF clutter artifacts. Consequently, these parts were correctly disposed of. However, an observer might now wrongly assume the absence of structural information in the corrupted area. Hence, it is always good practice to offer both pre- and post-filtered images to an observer. However, speckle tracking will not be corrupted further in these local dropout regions, since the original myocardial signal was already very weak. Compounding of multiple acquisitions obtained from spatially different positions might improve the CNR enough for the NF clutter reduction algorithm to spare the otherwise corrupted region, but this is beyond the scope of this current study.

Furthermore, in some frames, a small segment of the myocardium was wrongly mitigated by the filter. The most likely cause is the segment being composed of small filaments regularly surrounded by a relatively thick haze of NF clutter. Consequently, this segment will be absent in the detail images of scales two until four. Hence, the small myocardial section is regarded as NF clutter and thus discarded.

The filter might be expandable to other US fields, given the clutter has a similar morphology as those observed in echocardiography. Although, the filter proposed should be applicable using all phased- and curved-array probes, since the

environment of the imaged tissue is predominantly the determining factor in the NF clutter morphology [6], the frequency range of the probe employed might influence the appearance of the NF clutter.

This filter is designed for DICOM data, since DICOM data is clinically available. Nonetheless, the algorithm should be convertible to be also applicable for raw frequency data.

V. CONCLUSION

An NF clutter reduction algorithm has been introduced, which filters NF clutter artifacts in echocardiographic images based on their spatial-frequency characteristics using an oriented, multiscale approach. The algorithm successfully reduced NF clutter in all data sets of both the volunteer and the clinical study, resulting in enhanced image contrast. Furthermore, US speckles were preserved, which is a requirement for strain imaging. Moreover, the method proposed filters the images in the spatial frequency domain. Hence, the filter does not depend on differences in motion characteristics, which might be missing in infarcted areas or during end-diastole, and are limited in 3-D US. Therefore, the filter proposed is suitable for exercise stress echocardiography tests, and in patients with heart rhythm and contraction disorders.

VI. MULTIMEDIA FILES

Information on the prevalence of NF clutter in 3-D acquisitions is absent in literature. Therefore, a retrospective clinical data set was included containing 20 sets of 2-D and 3-D acquisitions obtained from a similar transducer position. The end-diastolic images of these acquisitions are shown in Fig. 8 in the multimedia files.

Fig. 3 only shows some representative results of the NF clutter reduction filter. Therefore, the NF clutter reduction results of the first end-diastolic volume of all 3-D data sets from the volunteer study (Fig. 9) and the clinical study (Fig. 10) have been included in the multimedia files.

Supplementary GIF files are provided containing four representative apical view data sets. Every file shows the original data set and the clutter reduced result in 3-D image slice planes, displayed over one cardiac cycle. Additionally, the longitudinal strain measurements of both the original and clutter reduced data set are included in the GIF files. Three out of the four GIF files show improved global longitudinal strain measurements post-NF clutter reduction, whereas the fourth GIF file shows a similar strain computation. The Supplementary Materials are available at http://ieeexplore.ieee.org.

REFERENCES

[1] F. Chirillo, "Impact of harmonic imaging on transthoracic echocardiographic identification of infective endocarditis and its complications," *Heart*, vol. 91, no. 3, pp. 329–333, Mar. 2005.

[2] B. C. Flynn, J. Spellman, C. Bodian, and V. K. Moitra, "Inadequate visualization and reporting of ventricular function from transthoracic echocardiography after cardiac surgery," *J. Cardiothoracic Vascular Anesthesia*, vol. 24, no. 2, pp. 280–284, Apr. 2010.

[3] C. Caiati, N. Zedda, C. Montaldo, R. Montisci, and S. Iliceto, "Contrast-enhanced transthoracic second harmonic echo Doppler with adenosine: A noninvasive, rapid and effective method for coronary flow reserve assessment," *J. Amer. College Cardiol.*, vol. 34, no. 1, pp. 122–130, 1999.

[4] M. Tanabe, B. Lamia, H. Tanaka, D. Schwartzman, M. R. Pinsky, and J. Gorcsan, "Echocardiographic speckle tracking radial strain imaging to assess ventricular dyssynchrony in a pacing model of resynchronization therapy," *J. Amer. Soc. Echocardiography*, vol. 21, no. 12, pp. 1382–1388, Dec. 2008.

[5] G. Zwirn and S. Akselrod, "Stationary clutter rejection in echocardiography," *Ultrasound Med. Biol.*, vol. 32, no. 1, pp. 43–52, Jan. 2006.

[6] A. Fatemi, E. A. R. Berg, and A. Rodriguez-Molares, "Studying the origin of reverberation clutter in echocardiography: *In vitro* experiments and *in vivo* demonstrations," *Ultrasound Med. Biol.*, vol. 45, no. 7, pp. 1799–1813, Jul. 2019.

[7] M. G. S. J. Sutton, J. D. Rutherford, and J. Leppo, *Clinical Cardiovascular Imaging: A Companion to Braunwald's Heart Disease*. Amsterdam, The Netherlands: Elsevier, 2004.

[8] S. N. Konstadt, S. K. Shernan, and Y. Oka, *Clinical Transesophageal Echocardiography: A Problem-Oriented Approach*. Philadelphia, PA, USA: Lippincott Williams & Wilkins, 2003.

[9] L. P. Badano, R. M. Lang, and J. L. Zamorano, *Textbook Real-Time Three Dimensional Echocardiography*. Cham, Switzerland: Springer, 2011.

[10] M. D. Puchalski et al., "Guidelines for performing a comprehensive transesophageal echocardiographic: Examination in children and all patients with congenital heart disease: Recommendations from the American society of echocardiography," *J. Amer. Soc. Echocardiography*, vol. 32, no. 2, pp. 173–215, 2019.

[11] Y. Yue, M. M. Croitoru, A. Bidani, J. B. Zwischenberger, and J. W. Clark, "Nonlinear multiscale wavelet diffusion for speckle suppression and edge enhancement in ultrasound images," *IEEE Trans. Med. Imag.*, vol. 25, no. 3, pp. 297–311, Mar. 2006.

[12] A. Pizurica, W. Philips, I. Lemahieu, and M. Acheroy, "A versatile wavelet domain noise filtration technique for medical imaging," *IEEE Trans. Med. Imag.*, vol. 22, no. 3, pp. 323–331, Mar. 2003.

[13] G. Andria, F. Attivissimo, A. M. L. Lanzolla, and M. Savino, "A suitable threshold for speckle reduction in ultrasound images," *IEEE Trans. Instrum. Meas.*, vol. 62, no. 8, pp. 2270–2279, Aug. 2013.

[14] K. Y. E. Leung, M. G. Danilouchkine, M. van Stralen, N. de Jong, A. F. W. van der Steen, and J. G. Bosch, "Probabilistic framework for tracking in artifact-prone 3D echocardiograms," *Med. Image Anal.*, vol. 14, no. 6, pp. 750–758, Dec. 2010.

[15] J. S. Turek, M. Elad, and I. Yavneh, "Clutter mitigation in echocardiography using sparse signal separation," *Int. J. Biomed. Imag.*, vol. 2015, pp. 1–18, 2015.

[16] F. W. Mauldin, D. Lin, and J. A. Hossack, "The singular value filter: A general filter design strategy for PCA-based signal separation in medical ultrasound imaging," *IEEE Trans. Med. Imag.*, vol. 30, no. 11, pp. 1951–1964, Nov. 2011.

[17] C. Demené et al., "Spatiotemporal clutter filtering of ultrafast ultrasound data highly increases Doppler and fultrasound sensitivity," *IEEE Trans. Med. Imag.*, vol. 34, no. 11, pp. 2271–2285, 2015.

[18] P. C. Tay, S. T. Acton, and J. A. Hossack, "A wavelet thresholding method to reduce ultrasound artifacts," *Computerized Med. Imag. Graph.*, vol. 35, no. 1, pp. 42–50, Jan. 2011.

[19] A. Yu and L. Lovstakken, "Eigen-based clutter filter design for ultrasound color flow imaging: A review," *IEEE Trans. Ultrason., Ferroelectr., Freq. Control*, vol. 57, no. 5, pp. 1096–1111, May 2010.

[20] R. S. Cobbold, *Foundations of Biomedical Ultrasound*. London, U.K.: Oxford Univ. Press, 2006.

[21] M. P. J. Kuenen, T. A. Saidov, H. Wijkstra, and M. Mischi, "Contrast-ultrasound dispersion imaging for prostate cancer localization by improved spatiotemporal similarity analysis," *Ultrasound Med. Biol.*, vol. 39, no. 9, pp. 1631–1641, Sep. 2013.

[22] R. S. Bandaru et al., "Speckle tracking of tendon displacement in the carpal tunnel: Improved quantification using singular value decomposition," *IEEE J. Biomed. Health Informat.*, vol. 23, no. 2, pp. 817–824, Mar. 2019.

[23] V. J. M. M. Schrier, S. Evers, J. G. Bosch, R. W. Selles, and P. C. Amadio, "Reliability of ultrasound speckle tracking with singular value decomposition for quantifying displacement in the carpal tunnel," *J. Biomech.*, vol. 85, pp. 141–147, Mar. 2019.

[24] E. P. Simoncelli and W. T. Freeman, "The steerable pyramid: A flexible architecture for multi-scale derivative computation," in *Proc. Int. Conf. Image Process.*, 1995, pp. 444–447.

[25] M. P. Sampat, Z. Wang, S. Gupta, A. C. Bovik, and M. K. Markey, "Complex wavelet structural similarity: A new image similarity index," *IEEE Trans. Image Process.*, vol. 18, no. 11, pp. 2385–2401, Nov. 2009.

[26] A. V. Oppenheim and J. S. Lim, "The importance of phase in signals," *Proc. IEEE*, vol. 69, no. 5, pp. 529–541, Dec. 1981.

[27] R. C. Gonzalez and R. E. Woods, "Image segmentation," in *Digital image Process.*, 3rd ed. New York NJ, USA: Pearson, 2008, pp. 742–747.

[28] S. Aja-Fernandez, R. S. J. Estepar, C. Alberola-Lopez, and C.-F. Westin, "Image quality assessment based on local variance," in *Proc. Int. Conf. IEEE Eng. Med. Biol. Soc.*, Aug. 2006, pp. 4815–4818.

[29] Z. Wang, A. C. Bovik, H. R. Sheikh, and E. P. Simoncelli, "Image quality assessment: From error visibility to structural similarity," *IEEE Trans. Image Process.*, vol. 13, no. 4, pp. 600–612, Apr. 2004.

[30] J. Lewis, "Industrial light & magic," *Fast Normalized Cross-Correlation*, Vol. 2011, Oct. 1995.

[31] P. Thavendiranathan, F. Poulin, K.-D. Lim, J. C. Plana, A. Woo, and T. H. Marwick, "Use of myocardial strain imaging by echocardiography for the early detection of cardiotoxicity in patients during and after cancer chemotherapy: A systematic review," *J. Amer. College Cardiology*, vol. 63, no. 25, Part A, pp. 2751–2768, 2014.

[32] K. Kusunose *et al.*, "Incremental prognostic value of left ventricular global longitudinal strain in patients with aortic stenosis and preserved ejection fraction," *Circulat., Cardiovascular Imag.*, vol. 7, no. 6, pp. 938–945, Nov. 2014.

[33] Y. Nagata *et al.*, "Prognostic value of LV deformation parameters using 2D and 3D speckle-tracking echocardiography in asymptomatic patients with severe aortic stenosis and preserved LV ejection fraction," *JACC, Cardiovascular Imag.*, vol. 8, no. 3, pp. 235–245, Mar. 2015.

[34] H. G. Carstensen, L. H. Larsen, C. Hassager, K. F. Kofoed, J. S. Jensen, and R. Mogelvang, "Basal longitudinal strain predicts future aortic valve replacement in asymptomatic patients with aortic stenosis," *Eur. Heart J. Cardiovascular Imag.*, vol. 17, no. 3, pp. 283–292, Mar. 2016.

[35] R. G. P. Lopata, M. M. Nillesen, H. H. G. Hansen, I. H. Gerrits, J. M. Thijssen, and C. L. de Korte, "Performance evaluation of methods for two-dimensional displacement and strain estimation using ultrasound radio frequency data," *Ultrasound Med. Biol.*, vol. 35, no. 5, pp. 796–812, May 2009.

[36] C. Jenkins, K. Bricknell, J. Chan, L. Hanekom, and T. H. Marwick, "Comparison of Two- and three-dimensional echocardiography with sequential magnetic resonance imaging for evaluating left ventricular volume and ejection fraction over time in patients with healed myocardial infarction," *Amer. J. Cardiology*, vol. 99, no. 3, pp. 300–306, Feb. 2007.

[37] F. Zhang, Y. M. Yoo, L. M. Koh, and Y. Kim, "Nonlinear diffusion in Laplacian pyramid domain for ultrasonic speckle reduction," *IEEE Trans. Med. Imag.*, vol. 26, no. 2, pp. 200–211, Feb. 2007.

[38] R. G. Dantas, E. T. Costa, and S. Leeman, "Ultrasound speckle and equivalent scatterers," *Ultrasonics*, vol. 43, no. 6, pp. 405–420, May 2005.

Sjoerd Bouwmeester received the Medical degree from the University of Maastricht, Maastricht, The Netherlands, in 2011. Thereafter, he started his specialist training in cardiology in Catharina Hospital, Eindhoven, The Netherlands, under the supervision of Dr. J. M. van Dantzig and Prof. Dr. N. H. J. Pijls.

He was registered as a Cardiologist in 2019, which was followed by a Fellowship in noninvasive cardiovascular imaging. Presently, he combines his fellowship with a Ph.D. trajectory under the supervision of Dr. P. Houthuizen and Prof. Dr. L. R. Dekker.

Patrick Houthuizen received the Medical degree from the Catholic University of Leuven, Leuven, Belgium, in 2011, and the Ph.D. degree in 2014. His Ph.D. thesis was entitled "Left Bundle Branch Block: Controversies in Aortic Valve Interventions and Cardiac Resynchronization Therapy," which was obtained at Maastricht University, The Netherlands.

Shortly after, he started working in Catharina Hospital, Eindhoven, The Netherlands, where he completed his cardiology training in 2009. As a cardiologist, he subspecialized in noninvasive cardiac imaging and valvular disease. He works in collaboration with the Eindhoven University of Technology, Eindhoven, with a focus on cardiac mechanics and ultrasound technology.

Frans N. van de Vosse received the M.Sc. degree in applied physics and the Ph.D. degree from the Eindhoven University of Technology (TU/e), Eindhoven, The Netherlands, in 1982 and 1987, respectively. His Ph.D. thesis is describing the numerical analysis of carotid artery flow.

From 1987 to 2001, he was a Lecturer in fluid mechanics with Materials Technology Group, TU/e Department of Mechanical Engineering. In 2001, he was appointed as a Full Professor in cardiovascular biomechanics with the Department of Biomedical Engineering (BMT), TU/e. His research interests are related to the computational and experimental biomechanical analysis of the cardiovascular system and its application to clinical diagnosis and intervention, cardiovascular prostheses, extracorporeal systems, and medical devices.

Marloes Sjoerdsma (Member, IEEE) received the B.Sc. degree in biomedical engineering from the Eindhoven University of Technology (TU/e), Eindhoven, The Netherlands, and the M.Sc. degree in medical engineering from TU/e in 2018 on the subject of hands-free, dynamic functional ultrasound. She is currently pursuing the Ph.D. degree in the field of multiperspective ultrasound of the cardiovascular system while she is performing research as a member of the Photoacoustics and Ultrasound Laboratory Eindhoven (PULS/e lab), TU/e, in collaboration with the Catharina Hospital, Eindhoven and Philips Research, Eindhoven.

Her research interests include all aspects of image (post) processing and functional imaging.

Richard G. P. Lopata (Senior Member, IEEE) received the M.Sc. degree in biomedical engineering from the Eindhoven University of Technology (TU/e), Eindhoven, The Netherlands, in 2004, with a focus on pharmacokinetic parameter estimation in dynamic contrast-enhanced MRI. From 2004 to 2009, he performed Ph.D. research at the Clinical Physics Laboratory of Radboudumc, Nijmegen, The Netherlands, resulting in his Ph.D. thesis on "2-D and 3-D Ultrasound Strain Imaging: Methods and *In Vivo* Applications."

He is currently an Associate Professor at TU/e. He founded and has been heading the research group "Photoacoustics and Ultrasound Laboratory Eindhoven" (PULS/e lab) since 2014. The PULS/e lab facilitates research on technology development, such as ultrasound functional imaging, photoacoustics, and image-based modeling; and more applied science, in particular ultrasound-based biomechanical modeling for improved clinical decision making.